X-ray standing wave method to study magnetism in crystals with site selectivity

Michał Kamiński,[1,*,†] Preeti Pokhriyal,[1] Heiko Schulz-Ritter,[1] Sonia Francoual,[1] Laurence Bouchenoire,[2,3] and Martin Tolkiehn[1]

[1]*Deutsches Elektronen-Synchrotron DESY, Notkestr. 85, 22607 Hamburg, Germany*

[2]*XMaS/BM28-ESRF, The European Synchrotron, 71 avenue des Martyrs, 38043 Grenoble Cedex 9, France*

[3]*Department of Physics, University of Liverpool, Oliver Lodge Laboratories, Oxford Street, Liverpool L69 7ZE, United Kingdom*

(Received 16 April 2025; revised 11 November 2025; accepted 22 January 2026; published 17 February 2026)

We report a new method for studying magnetism at the atomic level with site selectivity. It is based on the combination of the site-selective diffraction-based x-ray standing wave (XSW) technique and x-ray magnetic circular dichroism (XMCD), which provides the magnetic sensitivity. The use of the standing wave resulting from an interference between the incoming and the Bragg reflected electromagnetic waves ensures that the phase information is not lost and thus brings information about the magnetism at a given site directly. In the paper, we provide the theoretical foundations of such a method based on the dynamical theory of x-ray diffraction and time-dependent perturbation theory. By means of computer simulations, the principle of the method is thus presented in a rather accessible way. Finally, we demonstrate the results of a proof-of-principle experiment on single-crystalline yttrium-iron-garnet (YIG, $Y_3Fe_5O_{12}$). We show data exhibiting a clear variation in the XMCD signal caused by the standing wave. A comparison with theoretical functions illustrates that the established theory reliably describes the phenomena involved and allows to extract useful information about the magnetic moments in YIG.

DOI: 10.1103/tkb6-6qbx

I. INTRODUCTION

The fact that the phases of the scattered waves cannot be measured in a diffraction experiment has led in the past to the development of direct methods allowing to overcome this problem. Particularly elegant are the methods, which utilize the interference between the electromagnetic waves in order to actually measure the phase of the scattered wave. These include the three-beam-case diffraction [1,2], the x-ray standing wave (XSW) technique [3–5] and x-ray holography [6,7].

In the diffraction-based XSW technique, an interference field emerging in the Bragg reflection regime is used to study the positions of the atoms in an element-selective manner [8]. The standing wave ensures that the phase information is preserved and thus brings structural information directly. Until now, XSW has been mainly used to determine the structure of thin films and positions of dopants or surface adsorbates [4]. The canonical version of the XSW method, where the positions of the atoms are determined by recording the x-ray fluorescence yield [3], has been extended and combined with a number of other experimental techniques [5]. XSW was used, for instance, in conjunction with photoelectron spectroscopy (providing chemical state sensitivity), as well as Compton scattering (sensitive to low-Z elements) [9] and thermal diffuse scattering (providing information about phonons) [10].

Given the importance of magnetic materials for applications in modern electronics and the growing interest in magnetic nanostructures, the need for a method, which combines the magnetic sensitivity of x-ray magnetic circular dichroism (XMCD) with the spatial resolution at the atomic level of XSW has become crucial. XMCD [11,12] provides information about the magnitude of the net magnetic moments projected on the direction of the incident beam with element sensitivity. The use of diffraction-based x-ray standing waves provides additionally a crystallographic site-selectivity. Thanks to the spatial modulation of the electromagnetic radiation resulting from the wave's interference, one can selectively study the magnetism of individual magnetic sublattices, as long as the magnetic unit cell is the same as the atomic one (since the atomic structure determines the periodicity of the standing wave). The dependence of the XMCD signal on the angle between the light propagation direction and the magnetic moment opens up the possibility for studying the mutual orientation between the magnetic moments on the different sublattices.

It should be noted that apart from the atomic-resolution XSW, another version of this method was developed, where a standing wave formed in a layer or a multilayer by total reflection is used [13,14]. A combination of this XSW technique with XMCD has already been developed and experimentally tested on several systems [15–19]. Importantly,

*Contact author: michal.kaminski@kit.edu

†Present address: Karlsruhe Institute of Technology (KIT), Institute of Photon Science and Synchrotron Radiation (IPS), Hermann-von-Helmholtz-Platz 1, 76344 Eggenstein-Leopoldshafen, Germany.

the latter combination of techniques provides information about the magnetism of layers or interfaces, but not about the magnetism of atomic sites. That can be achieved only by utilizing a standing wave excited via Bragg reflection from the crystal lattice, which has the appropriate periodicity. The idea of a method that would be sensitive to the specific magnetic site was mentioned in two conference proceedings [20,21]. Here, we report a complete theoretical foundation of the method, illustrated by simulations of a model system. We show that with our theoretical approach, we are able to explain the data obtained for the yttrium-iron-garnet (YIG) single crystal and extract information about the orientations of the magnetic moments on magnetic sublattices, for the sample kept in an external magnetic field.

II. THEORY

From a theoretical perspective, the method can be reduced to the problem of scattering and absorption of an arbitrarily (usually circularly) polarized plane electromagnetic wave by a magnetized crystalline medium with magnetic ordering. The theoretical description of this process is built in two steps. At first, scattering of the wave by a crystal lattice is considered within the framework of the dynamical theory of x-ray diffraction [22–24], since only this formalism offers precise relations between the waves amplitudes and phases under the Bragg reflection regime. The absorption and dichroic effect are then described using quantum time-dependent perturbation theory [25,26], given that a nonrelativistic treatment suffices in the energy range of x-rays. Here only the most important results are summarized. A more detailed derivations are presented in the Supplemental Material (Sec. 1) [27].

A. Scattering of an arbitrarily polarized wave

The incoming wave $\boldsymbol{\mathcal{E}}_0^a$ is assumed to have the form of a monochromatic plane wave $\boldsymbol{\mathcal{E}}_0^a(\mathbf{r},t) = E_0^a(\varepsilon_\sigma \hat{\boldsymbol{\epsilon}}_\sigma + \varepsilon_\pi \hat{\boldsymbol{\epsilon}}_{0\pi})\mathrm{e}^{i\omega t - i\mathbf{k}_0^a\cdot\mathbf{r}}$, where E_0^a denotes the amplitude of the incoming wave, ω is the angular frequency, t denotes the time, $\mathbf{k}_0^a$ the incoming wave wave vector, and $\mathbf{r}$ the position vector. The polarization state is defined by the polarization vector $\boldsymbol{\epsilon}$, which corresponds to the expression in brackets, and more precisely by the polarization parameters ε_σ and ε_π. Without loss of generality ε_σ is assumed to be real, whereas ε_π is complex. For a circularly polarized wave, $\varepsilon_\sigma = 1/\sqrt{2}$ and $\varepsilon_\pi = i/\sqrt{2}$. The scattering process is described in the coordinate system $\mathcal{O}'$ shown in Fig. 1. $\mathbf{h}$ is the reciprocal lattice vector of the considered Bragg reflection, $\mathbf{k}_0$ and $\mathbf{k_h}$ are the wave vectors of the refracted and reflected waves, respectively. Those vectors define a scattering plane. The polarization unit vectors $\hat{\boldsymbol{\epsilon}}_\sigma$ (perpendicular to the scattering plane, along $\mathcal{O}y'$), $\hat{\boldsymbol{\epsilon}}_{0\pi}$ and $\hat{\boldsymbol{\epsilon}}_{\mathbf{h}\pi}$ (in the scattering plane, perpendicular to $\mathbf{k_0}$ and $\mathbf{k_h}$ respectively) are given mathematically by the relations $\hat{\boldsymbol{\epsilon}}_\sigma = (\mathbf{h}\times\mathbf{k}_0)/|\mathbf{h}\times\mathbf{k}_0| = (\mathbf{h}\times\mathbf{k_h})/|\mathbf{h}\times\mathbf{k_h}|$ and $\hat{\boldsymbol{\epsilon}}_{j\pi} = (\mathbf{k}_j\times\hat{\boldsymbol{\epsilon}}_\sigma)/|\mathbf{k}_j\times\hat{\boldsymbol{\epsilon}}_\sigma| = [\mathbf{k}_j\times(\mathbf{h}\times\mathbf{k}_j)]/(k_j|\mathbf{h}\times\mathbf{k}_j|)$, where $j = 0, \mathbf{h}$.

XSW experiments are generally performed in Bragg geometry. In the current treatment of the problem, we also assume the crystal to be thick enough, so that for each angular orientation in the vicinity of the reflection domain only one

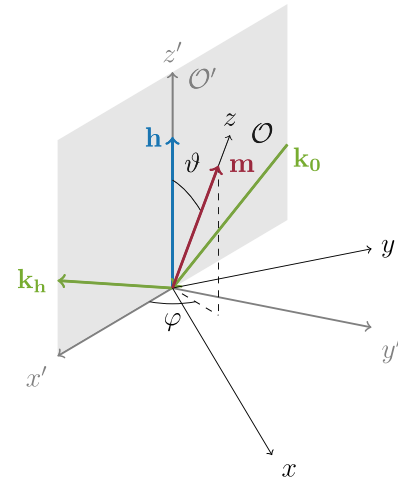

FIG. 1. The coordinate system $\mathcal{O}'$ (for scattering process) and $\mathcal{O}$ (for absorption process). The scattering plane is defined by the wave vectors of the incident ($\mathbf{k}_0$) and diffracted ($\mathbf{k_h}$) waves. The system $\mathcal{O}$ is defined by the magnetic moment ($\mathbf{m}$) direction. The relation between the coordinate systems $\mathcal{O}$ and $\mathcal{O}'$ is parametrized by the angles ϑ and φ. The choice of $\mathcal{O}x$ and $\mathcal{O}y$ is arbitrary.

wavefield is excited for a given σ- or π- polarization state [24]. More precisely, a potential second wavefield associated with a tiepoint lying on the other branch of the dispersion surface (indeed existing in a thin crystal) can only be excited by the reflection of the wavefield at the back surface of the crystal. Thus, this wavefield does not exist in the thick crystal as the wave is absorbed before it reaches the back surface. With those assumptions, one uses a standard formulation of the dynamical theory of x-ray diffraction [24], considering the boundary conditions separately for σ- and π-polarization states, and obtains the following expression for the intensity of the electromagnetic field (standing wave) in the crystal

$$I = |\boldsymbol{\mathcal{E}}|^2 = (E_0^a)^2\big\{\varepsilon_\sigma^2[1+|\xi_\sigma|^2 + 2\Re(\xi_\sigma \mathrm{e}^{-i\mathbf{h}\cdot\mathbf{r}})] + |\varepsilon_\pi|^2[1+|\xi_\pi|^2 + 2\Re(\xi_\pi \mathrm{e}^{-i\mathbf{h}\cdot\mathbf{r}})\cos 2\Theta_B]\big\}. \quad (1)$$

$\xi_\mathfrak{p} = E_{\mathbf{h}\mathfrak{p}}/E_{0\mathfrak{p}}$, $\mathfrak{p} = \sigma, \pi$, is an amplitude ratio, with $E_{\mathbf{h}\mathfrak{p}}$ and $E_{0\mathfrak{p}}$ being the amplitudes of the reflected and refracted waves in the crystal. The formula for $\xi_\mathfrak{p}$ is provided in Ref. [27].

Expression (1) is slightly simplified, since it was assumed that the difference in wave vectors for σ- and π-polarization components is small and that the complex part of the wave vector related to the absorption and extinction can be neglected. A complete expression can be obtained from the total electric field in the crystal $\boldsymbol{\mathcal{E}}$ provided in Ref. [27].

One should note that the intensity given by Eq. (1) depends on the angular orientation of the crystal, $I = I(\Delta\Theta)$, since $\xi_\mathfrak{p} = \xi_\mathfrak{p}(\Delta\Theta)$. $\Delta\Theta$ is the deviation angle from the orientation defined by Bragg's law (kinematical Bragg angle Θ_B), $\Delta\Theta = \Theta - \Theta_B$, where Θ is the angle between the incident wave direction and the diffracting lattice planes.

B. Absorption of an arbitrarily polarized wave

The interaction of a photon with an electron in the atom is modelled using a Pauli Hamilton operator [28]. The spin part is neglected, as well as terms containing a vector

potential in orders higher than first order [29,30]. An electric dipole approximation is adopted, as it suffices in most cases to correctly describe the absorption process occurring during the XSW and XMCD experiments [4,29,31].

According to Stoner's model of ferromagnetism of metals [32], when an ion possesses a net spin magnetic moment, the valence band exhibits a spontaneous spin polarization. This effect, together with the spin-orbit splitting of the final band, is responsible for the dichroism in absorption of the circularly or elliptically polarized light in ferromagnets.

Using the time-dependent perturbation theory to the first order and considering explicitly a difference in the density of unoccupied final states with opposite spin states, the total absorption cross-section reads [26,33]

$$\sigma = (4\pi)^2 \alpha_f \hbar\omega (\zeta^{\uparrow} \varrho_f^{\uparrow} + \zeta^{\downarrow} \varrho_f^{\downarrow}), \tag{2}$$

$\varrho_f^{m_s}$ is the density of empty final states with a given spin state $m_s = \pm\frac{1}{2}$ (where the abbreviations $\uparrow = \frac{1}{2}$ and $\downarrow = -\frac{1}{2}$ are used), α_f is the fine structure constant, and $\hbar$ is the reduced Planck constant. ζ^{m_s} are the spin-dependent transition rates given by the relation

$$\zeta^{m_s} = \sum_{if} |\langle f, m_s | \boldsymbol{\varepsilon}^* \cdot \mathbf{r} | \phi_i, m_s \rangle|^2. \tag{3}$$

They are calculated by considering the chosen transitions from the discrete initial states $|\phi_i\rangle$ to the final states $|f\rangle$, which form a continuum (for example, $2p \rightarrow 3d/5d$), and the operator $\boldsymbol{\varepsilon}^* \cdot \mathbf{r}$ expressed in terms of spherical harmonics, where $\boldsymbol{\varepsilon}^*$ is the complex conjugate of the polarization vector. More details are given in Ref. [27].

C. XMCD under the standing wave regime

In this section, the absorption cross-section is evaluated for the electromagnetic field of the standing wave, as derived from the dynamical theory of x-ray diffraction [Eq. (1)]. The direction of the magnetic moment sets the quantization axis for the considered problem. The relation between the coordinate systems $\mathcal{O}'$ and $\mathcal{O}$, Fig. 1, is given by the spherical angles ϑ and φ. This means that an arbitrary orientation between the magnetic moment of the atom and the scattering vector is considered. For the simplified case of the real wave vectors and $\mathbf{k}_{0\sigma} \approx \mathbf{k}_{0\pi} = \mathbf{k}_0$ the polarization vector derived from the dynamical theory of x-ray diffraction is equal to $[\varepsilon_\sigma \hat{\boldsymbol{\varepsilon}}_\sigma (1 + \xi_\sigma e^{-i\mathbf{h}\cdot\mathbf{R}}) + \varepsilon_\pi (\hat{\boldsymbol{\varepsilon}}_{0\pi} + \xi_\pi \hat{\boldsymbol{\varepsilon}}_{\mathbf{h}\pi} e^{-i\mathbf{h}\cdot\mathbf{R}})]$, where $\mathbf{R}$ is the position of the absorbing atom, as one considers the electric-dipole approximation. The attenuation of the emitted secondary signal (used to measure the absorption cross-section) on the way from the emitting atom to the detector is also neglected, something that is fully justified in the case of Auger electron yield detection or fluorescence detection with grazing detection angle [8].

The theoretical results are obtained based on an XMCD experiment performed at the $L_{2,3}$ absorption edges. This model is suitable for many of the magnetic systems, since they often contain $3d$ or $5d$ elements, whose magnetism can be studied by investigating the transitions $2p \rightarrow 3d/5d$ [12]. The XMCD signal for one atom is defined as a normalized difference between the absorption cross-sections for left-handed polarization (LHP, σ_L) and right-handed polarization (RHP, σ_R), $\Xi = (\sigma_L - \sigma_R)/(\sigma_L + \sigma_R)$. σ_L is calculated for the polarization state defined by ε_σ and ε_π ($\varepsilon_\pi = -i/\sqrt{2}$ for circular polarization) and σ_R for ε_σ and complex conjugate ε_π^* ($i/\sqrt{2}$ for circular polarization). By expressing the polarization vector $\boldsymbol{\varepsilon}^*$ in the scattering coordinate system $\mathcal{O}$ and calculating explicitly the transition rates ζ^{m_s} (details in Ref. [27]), one obtains

$$\Xi = \frac{\Pi_e^s \Sigma_1 \Delta\varrho_f^s}{I_{\mathrm{rel}} \varrho_f - \Pi_e^s \Psi_1 \Delta\varrho_f^s}, \tag{4}$$

where Π_e^s is a photoelectron spin polarization. This quantity depends on the transition considered in the experiment, or in other words on the absorption edge. For example, for the L_2 absorption edge $\Pi_e^s = -\frac{1}{2}$ and for L_3 $\Pi_e^s = \frac{1}{4}$. $\Delta\varrho_f^s$ is an imbalance in the spin-polarized density of the empty final states: $\Delta\varrho_f^s = \varrho_f^{\uparrow} - \varrho_f^{\downarrow}$, ϱ_f is the total density of final states: $\varrho_f = \varrho_f^{\uparrow} + \varrho_f^{\downarrow}$. The orbital polarization of the final band is neglected, but it can be incorporated into the theory in a similar manner as the spin polarization. I_{rel} indicates a relative intensity of the electric field, $I_{\mathrm{rel}} = I/(E_0^a)^2$, with I given by Eq. (1). For a simplified situation of circularly polarized incident wave ($\varepsilon_\sigma = 1/\sqrt{2}$ and $\varepsilon_\pi = i/\sqrt{2}$) and the magnetic moment in the scattering plane ($\varphi = 0$) and in the diffracting lattice planes ($\vartheta = \pi/2$), Ψ_1 vanishes and Σ_1 is given by the expression:

$$\Sigma_1 = \Re[(1 + \xi_\sigma e^{-i\mathbf{h}\cdot\mathbf{R}})(1 + \xi_\pi^* e^{i\mathbf{h}\cdot\mathbf{R}})] \cos\Theta_B. \tag{5}$$

This experimental situation is considered in Sec. III and most often also in the experiment reported in Sec. IV. General formulas for Σ_1 and Ψ_1 are given in Ref. [27]. Those terms are proportional to the spin polarization of the final band. Σ_1 is an expected circular polarization rate ($2\varepsilon_\sigma \Im\varepsilon_\pi$) supplemented by the terms emerging due to the interference between the waves, which grants a position sensitivity. The term Σ_1 vanishes for linearly polarized light ($\Im\varepsilon_\pi = 0 \Rightarrow \Sigma_1 = 0$). The term Ψ_1 does not vanish for linearly polarized light. It emerges due to the phase shifts induced under the diffraction regime. The σ- and π-polarized components of the incident wave are scattered differently, which changes the overall polarization of the wavefield inside the crystal (e.g., it does not maintain initial circular polarization).

In the real situation, there can be more than one magnetic atom per unit cell. This case is introduced by the summation of the absorption cross-sections in the numerator and denominator of Ξ. This yields the SW-XMCD signal Υ in the form

$$\Upsilon = \frac{\Pi_e^s \Sigma}{y - \Pi_e^s \Psi}, \tag{6}$$

where y is a secondary emission (electron or fluorescence) yield, within the electric dipole approximation, given by a sum of intensity at the positions $\mathbf{R}_j$ of n atoms of a given kind: $y = \frac{1}{n}\sum_{j=1}^{n} (I_{\mathrm{rel}})_j$. The quantities Σ and Ψ are defined also as normalized sums: $\Sigma = \frac{1}{n}\sum_{j=1}^{n} (\Sigma_1)_j (\Delta\varrho_f^s)_j/\varrho_f$, $\Psi = \frac{1}{n}\sum_{j=1}^{n} (\Psi_1)_j (\Delta\varrho_f^s)_j/\varrho_f$. Again, for a circularly polarized incident wave and the magnetic moment in the scattering and diffracting planes, Ψ vanishes and Σ takes the form

$$\Sigma = \left\{F_1^0 \left[1 + \Re\left(\xi_\sigma \xi_\pi^*\right)\right] + \Re\left[(\xi_\sigma + \xi_\pi)\left(F_1^{\mathbf{h}}\right)^*\right]\right\} \cos\Theta_B. \tag{7}$$

General formulas for y, Σ and Ψ are presented in the Supplemental Material [27]. The secondary radiation yield y is a function of a standing wave structure factor, defined by the sum $F_{sw}^{\mathbf{h}} = \frac{1}{n}\sum_{j=1}^{n} e^{i\mathbf{h}\cdot\mathbf{R_j}}$. F_k^0 and $F_k^{\mathbf{h}}$, $k = 1, 2, 3$ are coordinates of a new vector quantity, the magnetic standing wave structure factor. It is given by

$$\mathbf{F}_{msw}^{\mathbf{h}} = \frac{1}{n}\sum_{j=1}^{n} \mathbf{m}_j' e^{i\mathbf{h}\cdot\mathbf{R}_j}, \tag{8}$$

where prime by the magnetic moment $\mathbf{m}_j$ of the ion j indicates that its coordinates are given in the coordinate system $\mathcal{O}'$, in which the scattering process is described. $\mathbf{F}_{msw}^{0}$ is obtained by putting $\mathbf{h} = 0$ in (8).

When deriving Eq. (6), it was assumed that the total density of empty final states ϱ_f does not differ between atoms with different spin polarization, that is, different magnetic moments. According to the sum rules [31,34–36], the integral of the absorption cross-section over the energy is needed to calculate the magnetic moment. On the other hand, in other methods like magnetic holography [37,38] and magnetic small-angle x-ray scattering [39], an assumption about the proportionality between the XMCD signal at fixed energy and the magnetic moment is made. Therefore also here the ratio $(\Delta\varrho_f^s)/\varrho_f$ determined at fixed energy is identified with the magnitude of the magnetic moment of atom j. Consequently, even though the method does not allow to obtain absolute values of the magnetic moments, it still allows to observe differences between the magnetic moments of various atoms of the same element in the crystal.

Finally, for completeness, also the complex parts of the wave vectors are considered. Additionally, the effect of the attenuation of the emitted radiation on the way to the detector needs to be taken into account. The general formula for the SW-XMCD signal [Eq. (6)] remains the same, while the y, Σ, and Ψ change. The complete formulas are provided in Ref. [27].

III. EXAMPLE

In the standard XSW method, having the coordinates and atomic form factors (with dispersion corrections f' and f'' [40,41]), one can calculate an expected secondary emission yield. Assuming the directions and magnitudes of the magnetic moments and a photoelectron spin polarization Π_e^s, the expected SW-XMCD signal Υ can be calculated for any crystal. The function calculated numerically using this method and compared with experimentally determined angular-dependent XMCD signal, yields a direct information about the magnetic moments on sublattices.

A principle of the method is demonstrated using a model system, that is, a crystal doped with two magnetic ions, one located in between diffracting planes (hkl) of the crystal lattice (sublattice 1), and the other on the planes (sublattice 2). For calculations, a (111) reflection from perfect Si crystal at 7.1 keV was considered. It is assumed that there is an antiferromagnetic interaction between the sublattices and that the magnetic moment of the ion 1 is twice as big as that of ion 2 ($m_1 = -2m_2$), which corresponds to the model of a simple ferrimagnet. Both magnetic moments are parallel

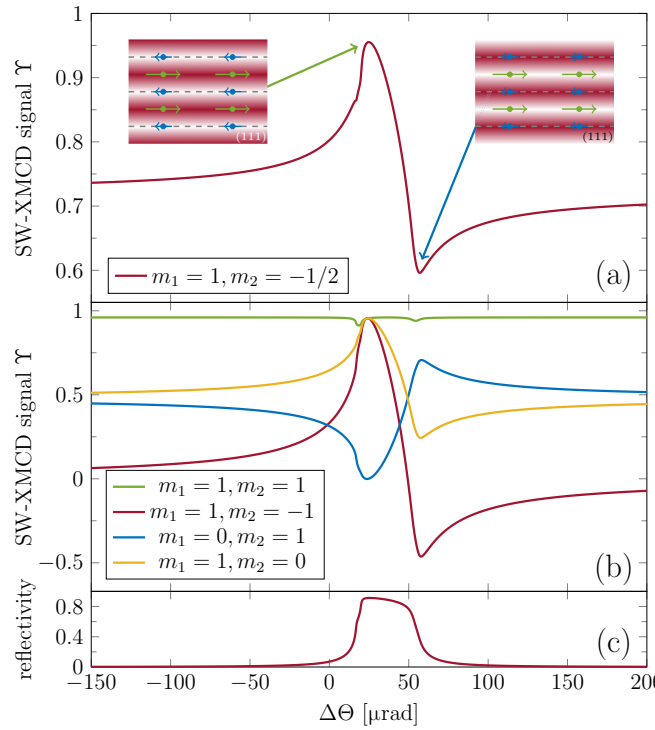

FIG. 2. (a) SW-XMCD signal as a function of deviation angle $\Delta\Theta$ for the model crystalline system with two magnetic dopants (one at the diffracting lattice planes and one in between) showing the principle of the method. The ions belonging to the sublattice 1 are marked in green, for the sublattice 2 in blue. The intensity of the standing wave is represented by the red/white color map in the insets, with red (white) meaning the maximum (minimum) intensity. On the low angular side of the reflection domain, the antinodes of the standing wave lie between the lattice planes and coincide with the green sublattice, yielding an increased XMCD signal. The XMCD signal is decreased when the standing wave maxima coincide with the blue atoms, and happens on the high angular side of the Bragg reflection. The shape of the variation is characteristic of this distribution of the magnetic moments. (b) The SW-XMCD signal for some other magnetic structures of the dopants. (c) The reflectivity $(\frac{1}{2}(|\xi_\sigma|^2 + |\xi_\pi|^2))$ curve for the considered Bragg reflection showing the angular region of the reflection domain.

to the diffracting lattice planes and in the scattering plane ($\vartheta = \pi/2$, $\varphi = 0$). For the simulations, the complex part of the wave vector was neglected, as well as the attenuation of the emitted secondary signal on the way to the detector. The incident beam was assumed to be circularly polarized and the photoelectron spin polarization Π_e^s set to 1 for simplicity. For numerical calculations, it is assumed that the largest magnetic moment is equal to 1. Equation (6) is given for this specific model in the Supplemental Material [27]. Also the values of $\mathbf{F}_{msw}^{\mathbf{h}}$ for the considered combinations of the magnetic moments of dopants are provided. The SW-XMCD signal for this selected Bragg reflection is shown in Fig. 2(a).

Away from the reflection domain, the observed XMCD signal is dictated by the net magnetic moment. This situation corresponds to the standard XMCD experiment. When the Bragg reflection is excited and the interference field

generated, the contribution of each of the sublattices to the measured dichroic signal changes. On the low angular side of the reflection domain, the standing wave antinodes lie in between lattice planes, enhancing the contribution of the sublattice 1. Since the direction of the net magnetic moment is the same as that of the ions 1, the XMCD signal increases. While the reflection domain is crossed, the phase of the reflected wave changes by π and consequently the standing wave moves by half of its period. That gradually increases the contribution of the sublattice 2, at the same time decreasing the contribution of the other one. On the high angular side of the reflection domain, the maxima of the electromagnetic field intensity coincide with the sublattice 2. The signal decreases, since the orientation of the magnetic moment of the ion 2 is opposite to the net magnetic moment. In a similar manner as in the standard XSW method, where the shape of the secondary emission yield is characteristic of the distribution of the atoms of a given kind, in this case, the shape of the variation in the XMCD signal is characteristic of the distribution of the magnetic ions.

The sensitivity of the method to the magnetic ordering can be visualized further by considering several other arrangements of the magnetic moments of the dopants. Four illustrative cases are shown in Fig. 2(b). The first arrangement (green curve) corresponds to the ferromagnetic structure, as the magnetic moments on both of the magnetic sublattices are the same. This fact is reflected in the lack of variation in the XMCD signal caused by the standing wave. Two small kinks are nevertheless observed, in relation with a change in the polarization and propagation directions of the waves. The change of the phase of the amplitude ratios causes changes in the overall wavefield polarization, which affects XMCD. Furthermore, the appearance of the reflected wave propagating in the other direction as the incident wave gives an additional contribution to the XMCD, different in magnitude from the background-level dichroism generated by the incident wave. In the second case (red curve), a net magnetic moment vanishes and corresponds to a pure antiferromagnet. Away from the reflection domain, the XMCD signal vanishes but because the standing wave can reduce the contribution from one sublattice and enhance the signal coming from the other one, a nonvanishing XMCD signal is observed under the Bragg reflection regime. The two other cases (blue and yellow curves) show the SW-XMCD signals for the case of one sublattice being nonmagnetic. The fact that either sublattice 1 (blue curve) or 2 (yellow curve) is nonmagnetic is reflected in the shape of the curve. In summary, the shape of the signal close to the Bragg reflection domain is very sensitive to the arrangement of the magnetic moments in the crystal lattice.

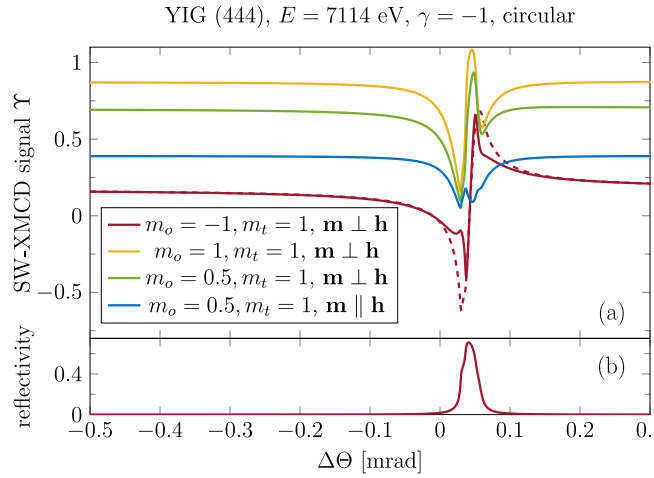

FIG. 3. (a) The simulated SW-XMCD signal for the YIG crystal. Several arrangements of the magnetic moments of the octahedrally (m_o) and tetrahedrally (m_t) coordinated Fe ions are considered. In each case, the magnetic moments are confined in the vertical scattering plane, their orientation with respect to the diffracting lattice planes (or vector **h**) is shown in the legend. The red curve corresponds to the spontaneous ferrimagnetic structure of YIG. For this case, the data calculated without taking into account the complex parts of the wave vectors and attenuation of the emitted secondary signal on the way to the detector (dashed red curve), and with these corrections (solid red curve), are compared. For the correction, it was assumed that the fluorescence detector is located above the sample ($\alpha = 90°$). All the other data were calculated with the correction. (b) The reflectivity curve for the (444) Bragg reflection.

IV. EXPERIMENTAL SECTION

A. Studied system

The experiments aiming to prove the feasibility of the method were performed on a (111) oriented single crystal of YIG ($Y_3Fe_5O_{12}$, lattice parameter 12.376 Å) [42]. Firstly, we show in Fig. 3 a collection of the simulated SW-XMCD signals for several arrangements of the magnetic moments in YIG. At room temperature, YIG exhibits a ferrimagnetic ordering with iron ions forming two sublattices. There are 16 octahedrally coordinated Fe^{3+} ions and 24 tetrahedrally coordinated ones, all exhibiting the same magnetic moment, but oriented oppositely between sublattices [43]. For the (444) Bragg reflection, the projection of the magnetic structure is such that the tetrahedrally coordinated ions lie on the diffracting lattice planes and octahedrally coordinated ones in between (see the inset in Fig. 4). The red curve is a simulated SW-XMCD signal for the spontaneous ferrimagnetic structure of YIG. The dashed curve was calculated without taking into account the complex parts of the wave vectors and attenuation of the emitted secondary signal on the way to the detector. The solid curve was calculated with this correction and assuming that the secondary signal (fluorescence) detector is located above the sample ($\alpha = 90°$). One can notice a rather minor difference between those two, what owes to the fact that a normalized signal is considered (difference in absorption cross-sections divided by the sum) and that the correction factor does not depend strongly on the helicity and magnetic moment orientation. The rest of the data were calculated including these corrections. The yellow and green curves correspond to the ferromagnetic ordering, the latter for a magnetic moment of the octahedrally coordinated ions halved that of the tetrahedrally coordinated ones. The blue curve was calculated for the latter case, but with the magnetic moments perpendicular to the diffracting lattice planes.

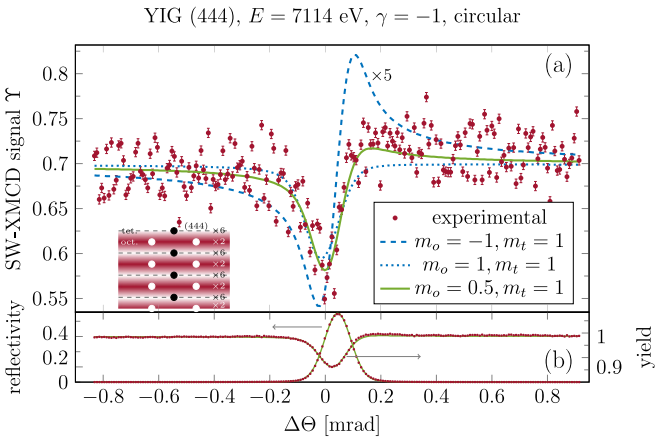

FIG. 4. Experimental data for the YIG (444) Bragg reflection compared with theoretical results. The magnetic field was oriented in the vertical scattering plane and perpendicular to the reciprocal lattice vector $\mathbf{h}_{(444)}$ of the reflection. (a) SW-XMCD signal as a function of deviation angle compared with the theoretical curves for three values of the magnetic moment m_o of the octahedrally coordinated ions. The data were normalized by the theoretical value of SW-XMCD (green curve) for $\Delta\Theta \to \pm\infty$. For clarity, the curve for a ferrimagnetic structure ($m_o = -1$, $m_t = 1$, dashed blue) was shifted to zero, scaled by 0.2 and shifted back to the XMCD background level to fit it in the graph. The best agreement is obtained for m_o two times shorter than the magnetic moment of the tetragonally coordinated ions m_t (green curve). This might be attributed to the incomplete suppression of the antiferromagnetic coupling between sublattices in an external magnetic field. For more explanation, see the text. (b) Diffraction rocking curve (left scale) and fluorescence yield (right) for one of the configurations of helicity and magnetic field orientation, together with theoretical curves. The inset in (a) shows schematically the cut through the YIG lattice with Fe sublattices (white points: octahedrally coordinated ions, black points: tetrahedrally) and (444) lattice planes. The red color gradient symbolizes the standing wave existing in the crystal on the low angular side of the reflection domain.

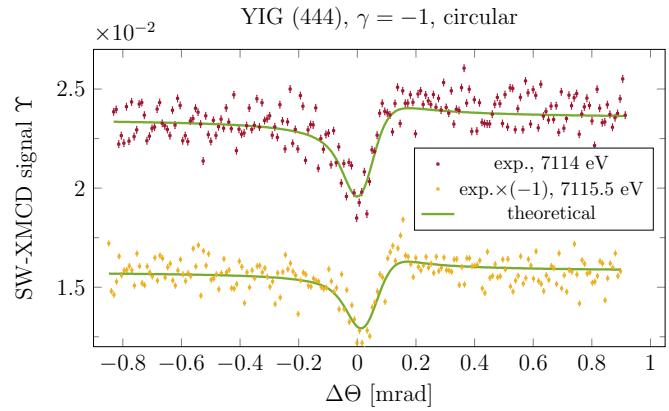

FIG. 5. Comparison between data obtained for the YIG (444) Bragg reflection at 7114 and 7115.5 eV (both around the pre-edge resonance). The theoretical curves are shown for both cases. As expected, the magnetic signal observed at those two energies is reversed and in the case of 7115.5 eV, around 1.5 lower than at 7114 eV. Most importantly, the shape of the signal in the reflection domain remains the same regardless of energy, which justifies a measurement at a fixed energy value.

B. Experimental details

The experiments were performed at the P09 beamline [44] at PETRA III light source at DESY, Hamburg and at the BM28 (XMaS) beamline [45] at ESRF. The data presented here come from the beamtime at P09, where the sample was mounted on a 6-circle diffractometer and magnetized with a permanent magnet system with variable field direction providing around 250 mT, designed at DESY [46]. The change of the magnetic field direction is possible remotely via a motorized rotation of the permanent magnets. The beam spot on the sample was $0.12 \times 0.2\,\text{mm}^2$ (V × H). The diffracted beam intensity was measured by an avalanche photodiode (APD), whereas the fluorescence spectra were collected with a silicon drift diode (SDD) detector (Amptek, Inc., USA) located above the sample surface ($\alpha = 90^\circ$). This setting ensures a higher count-rate, what is crucial given a very weak XMCD signal at the K absorption edge. The beam was circularly polarized using phase retarder plates [47,48]. The helicity of the beam was fast switched between the RHP and LHP states at a frequency of 23 Hz, and the signals corresponding to those different polarization states were recorded synchronously. The scans were performed with circularly polarized incoming beam, whose polarization degree was measured to be $99.8 \pm 0.1\%$ and $99.1 \pm 0.2\%$ for the two settings of the phase plate corresponding to LHP and RHP. The experiment was performed at room temperature.

The data collection consisted of orienting a sample at a chosen Bragg reflection and while performing a rocking scan recording a full fluorescence spectrum at each angular step, as well as the diffracted beam intensity. Given the weakness of the XMCD effect at the iron K absorption edge, the counting time was 10 s per point and each scan was repeated at least 10 times. The XSW-excited iron fluorescence signal for each helicity was extracted from the total fluorescence spectra by subtracting the background, fitting a Gaussian function and integrating the spectral line corresponding to the Fe K_α emission. The yield was normalized by the incoming beam monitor. In order to ensure the magnetic origin of the observed difference in fluorescence yields $\sigma_{L/R}$ recorded for each helicity, additionally the sample was magnetized and the orientation of the magnetic field reversed by 180° after each full angular scan. That provided four types of fluorescence yields, $\sigma_{L/R}^{\pm B}$, which were used to calculate the SW-XMCD signal as a difference $\Upsilon_{\text{exp}} \propto (\sigma_L^{+B} - \sigma_R^{+B})/(\sigma_L^{+B} + \sigma_R^{+B}) - (\sigma_L^{-B} - \sigma_R^{-B})/(\sigma_L^{-B} + \sigma_R^{-B})$. This procedure was crucial, since a strong nonmagnetic $\Delta\Theta$-dependent signal in $(\sigma_L - \sigma_R)/(\sigma_L + \sigma_R)$ was observed, whose origin remains unknown. By performing scans away from the absorption edge (100 eV above) and observing the vanishing of Υ_{exp}, we ensured that it is of purely magnetic origin. The correspondence between Eq. (6) and Υ_{exp} is discussed in details in Ref. [27]. The SW-XMCD signal as shown in Figs. 4, 6, and 7 was normalized to the value for $\Delta\Theta \to \pm\infty$ of the theoretical curve for the arrangement of the magnetic moments which was found to best reproduce the data. The average experimental values of SW-XMCD for $\Delta\Theta \to \pm\infty$ before normalization are given in Supplemental Material (Table S1) [27]. In case of Fig. 5,

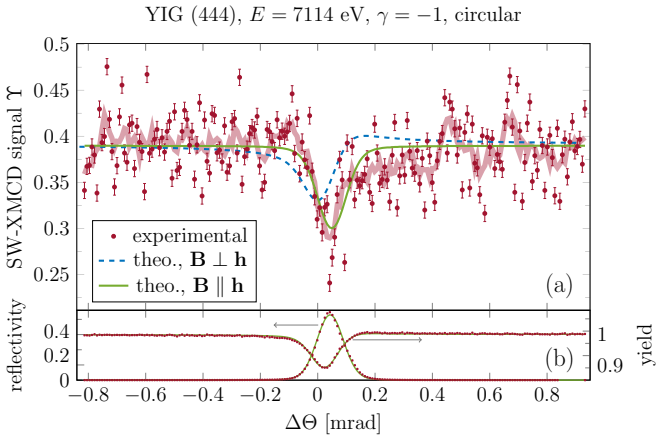

FIG. 6. Experimental data for the YIG (444) Bragg reflection compared with theoretical results. The red semi-transparent line shows the moving average of the observed data points. The same experimental parameters as in Fig. 4, but now the magnetic field was oriented along the reciprocal lattice vector $\mathbf{h} = (444)$. (a) SW-XMCD signal compared with the theoretical curves, the one for $\mathbf{B} \perp \mathbf{h}$ is shown for comparison. The data were normalized by the theoretical value of SW-XMCD for $\Delta\Theta \to \pm\infty$. (b) Reflectivity curve (left scale) and fluorescence yield (right) for one of the settings of helicity and magnetic field orientation, together with theoretical curves.

the data were not normalized as the purpose here is to show the behavior of the signal at different energies.

One of the aims of the experiment at BM28 was to verify the results obtained at P09. The experimental conditions were essentially the same and the results confirmed the findings from the measurements performed at P09.

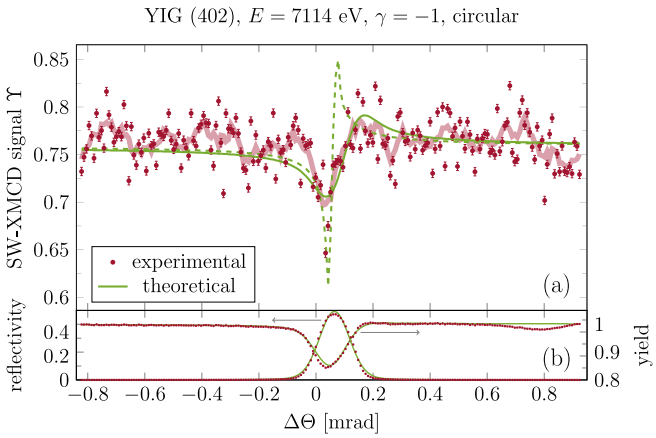

FIG. 7. Experimental data for the YIG (402) Bragg reflection compared with theoretical results. The red semitransparent line shows the moving average of the observed data points. The magnetic field was in the vertical scattering plane and perpendicular to the reciprocal lattice vector $\mathbf{h}_{(402)}$ of the reflection. (a) SW-XMCD signal compared with the theoretical curve. The data were normalized by the theoretical value of SW-XMCD for $\Delta\Theta \to \pm\infty$. Because of a high noise level, assessment of the fit quality is difficult, and thus a theoretical curve without a convolution with a Gaussian function is also shown (dashed). (b) Reflectivity curve (left scale) and fluorescence yield (right) for one of the settings of helicity and magnetic field orientation, together with theoretical curves.

V. RESULTS AND DISCUSSION

Firstly we studied the (444) Bragg reflection ($\Theta_B^{(444)} = 29.2°$, lattice planes spacing $d_{(444)} = 1.786$ Å), given a very convenient projection of the magnetic structure (as shown in the inset of Fig. 4). The energy was tuned to 7114 eV, corresponding to the pre-edge feature of the YIG absorption spectrum where the XMCD signal is expected to be the highest [49,50]. For the measured x-ray absorption spectrum, see Ref. [27]. The resulting SW-XMCD signal, the fluorescence yield for one of the four configurations of the magnetic field and beam helicity, and the diffracted beam intensity are shown in Fig. 4. The first observation is a clear variation in the XMCD across the reflection domain, implying the impact of the standing wave.

In order to reach a good agreement with the experimental diffraction rocking curve, the theoretical rocking curve was convolved with a Gaussian function accounting for the incoming beam divergence and energy spread, as well as the crystal mosaicity. The parameters of the Gaussian function were determined by minimising the difference between the theoretical function and the experimental data. The same procedure was repeated for the fluorescence yield and SW-XMCD signal; the width of the Gaussian function used was the one obtained from the fits to the diffracted intensity curve. The width parameter obtained from the fit is equal 0.106 mrad and results mostly from the crystal's mosaicity. The structural parameters were adjusted manually, and the quality of agreement between the theoretical function and the experimental data was assessed visually. The experimental data could not be fitted using standard literature values of the anomalous corrections f' and f'' for Fe [41]. Good agreement was only obtained with the theoretical function calculated using the absorption correction f'' for the octahedrally coordinated iron ions multiplied by 4. A possible reason for introducing this correction might be related to the fact that the tabulated values are given for pure elements and that the crystal environment affects the absorption probabilities. It is known that the absorption cross-section (and thus also f'') in the vicinity of the absorption edge is very sensitive to the oxidation state and local environment of the ion. Therefore it is expected that the tabulated values may not correspond to the real ones for ions in a complex crystal environment like the one in YIG. With our experiment and analysis procedure, we provide more realistic values for the anomalous corrections for the iron ions in YIG in the vicinity of the K absorption edge. The correction of the literature values was not necessary for control scans performed 100 eV above the absorption edge ($E = 7214$ eV).

The theoretical curve, that is a function calculated based on Eq. (6) and convolved with Gaussian function as described in the previous paragraph, (for more details and fit parameters, see the Supplemental Material [27]) shown in Fig. 4 for the ferrimagnetic structure of YIG (dashed line, $m_t = 1$, $m_o = -1$, where m_j, $j = t, o$ denotes normalized magnetic moments for tetrahedrally and octahedrally coordinated ions respectively), does not reproduce the SW-XMCD signal observed experimentally. The variation is expected to

be significant due to the large difference in magnetic moments between sublattices in a ferrimagnet. Since the sample was kept in an external magnetic field of 250 mT, the antiferromagnetic coupling between sublattices was very likely suppressed. This is supported by previous studies reporting a saturation magnetization for YIG of around 200 mT [51]. A much better agreement is reached assuming a ferromagnetic ordering with all the magnetic moments aligned along an applied external magnetic field (dotted line). The best agreement with experimental data was achieved assuming a slightly smaller magnetic moment on the less populated sublattice with octahedrally coordinated iron atoms, which might indicate an incomplete reversal of the moments' orientations. This hypothesis is confirmed by a simulation with the magnetic moments of that sublattice tilted by 40° to the (444) lattice planes that gave a similar good agreement.

Another set of scans was performed with the same parameters at an energy 1.5 eV higher ($E = 7115.5\,\text{eV}$, $\Theta_B^{(444)} = 29.19°$), where the XMCD signal from YIG is expected to be reversed and around half of that expected at $E = 7114\,\text{eV}$ [49,50]. One can see in Fig. 5 that the signal is reversed as expected and found to be 1.5 times weaker away from the reflection domain. Additionally, the shape of the signal in the reflection domain remained unchanged, implying that scans can be performed at a single energy. Measurements were repeated for an elliptically polarized incoming beam (circular polarization rate $38.5 \pm 0.4\%/38.1 \pm 0.4\%$ for opposite helicities). They revealed a decrease of the SW-XMCD signal away from the reflection domain by 44% with respect to circular polarization and no change in the shape of the variation, in agreement with the simulations.

Since the method is sensitive to the orientation of the magnetic moments, a series of scans was performed at 7114 eV with the same diffraction condition, but with the magnetic field oriented perpendicular to the (444) diffracting lattice planes. Figure 6 presents the experimental data and theoretical curves for that configuration. The solid line is the one showing the best agreement and was calculated assuming the magnetic moments along $\mathbf{h}_{(444)}$ and the same as in the previous case, that is halved for the Fe atoms with octahedral coordination. The dashed curve is the one when the magnetic moments are aligned in the diffracting lattice planes. One can see that the variation is higher in the considered case, since the magnetic moments are oriented further away from the direction of the incoming beam and thus the reflected beam imposes greater change as in the case of $\mathbf{B} \perp \mathbf{h}$.

Finally, the experiment was repeated for another Bragg reflection, (402) ($\Theta_B^{(402)} = 18.35°$, $d_{(402)} = 2.767\,\text{Å}$). The crystal was oriented such that the normal to the surface was bisecting the angle between incoming and reflected beams, that is, the Bragg reflection was still symmetric ($\gamma = -1$). The magnetic field was still in the scattering plane and in the plane of the sample surface. For this geometry $\mathbf{B} \perp \mathbf{h}_{(402)}$, the data were presented in Fig. 7. In this case, the tabulated absorption correction f'' had to be multiplied by 7 for the octahedrally coordinated iron ions in order to achieve a good agreement with experimental data. A small decrease in the yield far from the reflection domain on the high angular side is a manifestation of another Bragg reflection. The diffracted wave is not directed towards the point detector and thus manifests itself only in fluorescence yield. It did not influence the signal in the (402) reflection domain. In this case also, the assumption of smaller magnetic moments for the octahedrally coordinated ions led to the best agreement between calculated and observed curves. Because of a high noise level, assessment of the fit quality is difficult and thus apart from a curve resulting from a convolution with a Gaussian function, a theoretical curve calculated directly based on Eq. (6) is shown in Fig. 7. The scaling of the theoretical curve to the XMCD signal level away from the reflection domain is also nonideal due to high noise.

VI. CONCLUSIONS

We have presented the foundations of a direct method for studying the magnetism of crystalline materials with site-selectivity. The position sensitivity is granted by the standing wave resulting from the interference between the incident and Bragg reflected waves. On the other hand, the magnetic properties are probed using XMCD. The shape of the variation as a function of the deviation angle in the latter caused by the standing wave allows to probe the magnetic moments of different sublattices. The theoretical description of the method includes the most general case of multiple magnetic atoms in the unit cell with arbitrary orientations of the magnetic moments, and equations (shown in Sec. II.3) were derived for the first time.

As we conclude from the theory, experimentally the XMCD signal under the standing wave regime can be determined by collecting two fluorescence yields during the rocking scan, for opposite helicities of the incoming beam. We have chosen YIG as a test system to demonstrate the feasibility of the method. In our case, the sample was magnetised in an external magnetic field to avoid nonmagnetic contributions to the differential signal. We have collected a number of datasets for (444) and (402) Bragg reflections. The scans were performed at the pre-edge, at two energies (7114 eV and 7115.5 eV) corresponding to two extrema in the XMCD. We have observed an expected reversal and, more importantly, no change in the shape of the SW-XMCD signal. A scan performed away from the absorption edge confirmed the magnetic origin of the signals. The magnetic field was oriented either parallel or perpendicular to the diffracting lattice planes. We also used an elliptically polarised incoming beam. Despite the high noise level owing to the weakness of the XMCD at the K absorption edge, we could explain all the data using the developed theory. We assumed a suppression of the antiferromagnetic coupling between the two iron sublattices in YIG and half the size magnetic moment at the octahedrally coordinated ions compared to the magnetic moment at the tetrahedrally coordinated ones. The latter can be explained by an incomplete alignment in the magnetic field. In comparison with the standard XMCD method, which gives information on the net magnetic moment with element selectivity, our findings imply that XMCD combined with atomic-resolution XSW provides additional information with site-selectivity.

The method could potentially provide useful information about magnetism in thin films, which is not easily accessible with neutron diffraction due to the small scattering cross-sections. Samples have to be of high crystalline quality, and

the magnetic elements have to exhibit absorption edges (ideally L edges) in the hard x-ray regime. In order to extract useful information, the magnetic unit cell should match the atomic unit cell, since the atomic lattice generates the standing wave. If these conditions are fulfilled, the presented method directly yields magnetic information. It could possibly probe changes in the magnetic ordering depending on the temperature or the magnetic field magnitude/direction. We foresee that due to the interference field, one would also be able to observe an XMCD effect from an antiferromagnet.

ACKNOWLEDGMENTS

We acknowledge DESY (Hamburg, Germany), a member of the Helmholtz Association HGF, for the provision of experimental facilities. Parts of this research were carried out at PETRA III, and we would like to thank Julian Burkhardt and Jose R. L. Mardegan for assistance in using P09. Beamtime was allocated for proposals I-20210835 and I-20220252. We acknowledge the European Synchrotron Radiation Facility (ESRF) for the provision of beamtime under proposal No. HC-5109, and we would like to thank Didier Wermeille, Paul Thompson, and Oier Bikondoa for assistance and support in using beamline BM28 (XMaS). M.K. would like to thank Edgar Weckert, Sebastian Thieß, and Andreas Stierle for many fruitful discussions and Markus Tischer for the help with the development of the magnet system.

DATA AVAILABILITY

The data that support the findings of this article are not publicly available upon publication because it is not technically feasible and/or the cost of preparing, depositing, and hosting the data would be prohibitive within the terms of this research project. The data are available from the authors upon reasonable request.

[1] S.-L. Chang, Direct determination of x-ray reflection phases, Phys. Rev. Lett. **48**, 163 (1982).
[2] E. Weckert and K. Hümmer, Multiple-beam x-ray diffraction for physical determination of reflection phases and its applications, Acta. Crystallogr. A **53**, 108 (1997).
[3] B. W. Batterman, Detection of foreign atoms by their x-ray fluorescence scattering, Phys. Rev. Lett. **22**, 703 (1969).
[4] J. Zegenhagen, Surface structure determination with x-ray standing waves, Surf. Sci. Rep. **18**, 202 (1993).
[5] Edited by J. Zegenhagen and A. Kazimirov, *The X-Ray Standing Wave Technique. Principles and Applications* (World Scientific, Singapore, 2013).
[6] A. Szöke, X-ray and electron holography using a local reference beam, AIP Conf. Proc. **147**, 361 (1986).
[7] K. Hayashi and P. Korecki, X-ray fluorescence holography: Principles, apparatus, and applications, J. Phys. Soc. Jpn. **87**, 061003 (2018).
[8] J. Zegenhagen and A. Kazimirov, X-ray standing waves in a nutshell, in *The X-Ray Standing Wave Technique. Principles and Applications*, edited by J. Zegenhagen and A. Kazimirov (World Scientific, Singapore, 2013).
[9] M. K. Tiwari, H. Wang, K. J. S. Sawhney, M. Nayak, and G. S. Lodha, X-ray standing wave induced Compton and elastic scattering from thin periodic multilayer structures, Phys. Rev. B **87**, 235401 (2013).
[10] H. Spalt, A. Zounek, B. N. Dev, and G. Materlik, Coherent x-ray scattering by phonons: Determination of phonon eigenvectors, Phys. Rev. Lett. **60**, 1868 (1988).
[11] J. Stöhr and Y. Wu, X-ray magnetic circular dichroism: Basic concepts and theory for 3d transition metal atoms, in *New Directions in Research with Third-Generation Soft X-Ray Synchrotron Radiation Sources*, edited by A. S. Schlachter and F. J. Wuilleumier (Kluwer Academic Publishers, Dordrecht, 1994).
[12] J. Stöhr, Exploring the microscopic origin of magnetic anisotropies with x-ray magnetic circular dichroism (XMCD) spectroscopy, J. Magn. Magn. Mater. **200**, 470 (1999).
[13] M. J. Bedzyk, X-ray standing wave at the total reflection condition, in *The X-Ray Standing Wave Technique. Principles and Applications*, edited by J. Zegenhagen and A. Kazimirov (World Scientific, Singapore, 2013).
[14] M. J. Bedzyk and J. A. Libera, X-ray standing wave in multilayers, in *The X-Ray Standing Wave Technique. Principles and Applications*, edited by J. Zegenhagen and A. Kazimirov (World Scientific, Singapore, 2013).
[15] S.-K. Kim and J. B. Kortright, Modified magnetism at a buried Co/Pd interface resolved with x-ray standing waves, Phys. Rev. Lett. **86**, 1347 (2001).
[16] S.-H. Yang, B. S. Mun, N. Mannella, S.-K. Kim, J. B. Kortright, J. Underwood, F. Salmassi, E. Arenholz, A. Young, Z. Hussain, M. A. V. Hove, and C. S. Fadley, Probing buried interfaces with soft x-ray standing wave spectroscopy: Application to the Fe/Cr interface, J. Phys.: Condens. Matter **14**, L407 (2002).
[17] K. Sato, M. Sugawara, T. Jinno, M. Toyoda, T. Hatano, A. Arai, and M. Yanagihara, X-ray magnetic circular dichroism studies for Fe/Si interfaces using standing waves, J. Phys.: Conf. Ser. **83**, 012012 (2007).
[18] M. A. Andreeva and E. E. Odintsova, X-ray circular dichroism under reflection from antiferromagnetically coupled multilayers, Moscow Univ. Phys. **67**, 196 (2012).
[19] P. Jonnard, M. Wu, J.-M. André, K. L. Guen, F. Schäfers, A. Sokolov, E. Filatova, A. Verna, Z. Wang, and Q. Huang, Dichroism of x- ray fluorescence under standing waves regime in magnetic periodic multilayers, https://hal.science/hal-01783440v1.
[20] H. Kawata, T. Iwazumi, N. Shiotani, and F. Itoh, First measurement of site-specific normal and magnetic XANES by using a standing wave field, in *Resonant Anomalous X-Ray Scattering. Theory and Applications*, edited by G. Materlik, C. J. Sparks, and K. Fischer (Elsevier Science B.V., Amsterdam, 1994).
[21] N. Jaouen, F. Whilhelm, A. Rogalev, and J. Goulon, Magnetism of impurities probed with x-ray standing waves, AIP Conf. Proc. **879**, 1707 (2007).
[22] M. von Laue, *Röntgenstrahl-Interferenzen* (Akademische Verlagsgesellschaft, Frankfurt am Main, 1960).

[23] B. W. Batterman and H. Cole, Dynamical diffraction of x rays by perfect crystals, Rev. Mod. Phys. **36**, 681 (1964).

[24] A. Authier, *Dynamical Theory of X-Ray Diffraction* (Oxford University Press, Oxford, 2001).

[25] P. A. M. Dirac, On the theory of quantum mechanics, Proc. Roy. Soc. A **112**, 661 (1926).

[26] C. Cohen-Tannoudji, B. Diu, and F. Laloë, *Quantum Mechanics* (Hermann, Paris, 1977).

[27] See Supplemental Material at http://link.aps.org/supplemental/10.1103/tkb6-6qbx for the detailed derivation of the formulas from theoretical section; explicit expressions for the used quantities from the dynamical theory of x-ray diffraction; most general formulas for the SW-XMCD signal for one and many atoms, also including the correction for the complex parts of the wave vectors and the effect of the attenuation of the emitted radiation on the way to the detector; the explicit expressions for SW-XMCD and values of $\mathbf{F}_{msw}$ used for simulations and analysis of the experimental data; how the experimental SW-XMCD signal is related to the one given by formula (6); the experimental values of SW-XMCD for $\Delta\Theta \to \pm\infty$; the measured x-ray absorption spectrum of YIG; the parameters of the Gaussian functions used in the data analysis.

[28] W. Pauli, Jr., Zur quantenmechanik des magnetischen elektrons, Z. Phys. **43**, 601 (1927).

[29] F. Baudelet, X-ray magnetic circular dichroism, in *Neutron and X-ray Spectroscopy*, edited by F. Hippert, E. Geissler, J. L. Hodeau, E. Lelièvre-Berna, and J. R. Regnard (Springer, Dordrecht, 2006).

[30] A. Fontaine, Interaction of x-rays with matter: X-ray absorption spectroscopy, in *Neutron and Synchrotron Radiation for Condensed Matter Studies. Volume I. Theory, Instruments and Methods*, edited by J. Baruchel, J. L. Hodeau, M. S. Lehmann, J. R. Regnard, and C. Schlenker (EDP Sciences - Springer-Verlag, Berlin, 1993).

[31] S. W. Lovesey and S. P. Collins, *X-Ray Scattering and Absorption by Magnetic Materials* (Clarendon Press, Oxford, 1996).

[32] E. C. Stoner, Collective electron ferromagnetism, Proc. Roy. Soc. A **165**, 372 (1938).

[33] P. A. M. Dirac, The quantum theory of the emission and absorption of radiation, Proc. Roy. Soc. A **114**, 243 (1927).

[34] B. T. Thole, P. Carra, F. Sette, and G. van der Laan, X-ray circular dichroism as a probe of orbital magnetization, Phys. Rev. Lett. **68**, 1943 (1992).

[35] P. Carra, B. T. Thole, M. Altarelli, and X. Wang, X-ray circular dichroism and local magnetic fields, Phys. Rev. Lett. **70**, 694 (1993).

[36] J. Stöhr and H. C. Siegmann, *Magnetism. From Fundamentals to Nanoscale Dynamics* (Springer-Verlag, Berlin, Heidelberg, 2006).

[37] S. Eisebitt, J. Lüning, W. F. Schlotter, M. Lörgen, O. Hellwig, W. Eberhardt, and J. Stöhr, Lensless imaging of magnetic nanostructures by x-ray spectro-holography, Nature (London) **432**, 885 (2004).

[38] C. Tieg, R. Frömter, D. Stickler, S. Hankemeier, A. Kobs, S. Streit-Nierobisch, C. Gutt, G. Grübel, and H. P. Oepen, Imaging the in-plane magnetization in a Co microstructure by Fourier transform holography, Opt. Express **18**, 27251 (2010).

[39] P. Fischer, R. Zeller, G. Schütz, G. Goerigk, and H.-G. Haubold, Magnetic small angle x-ray scattering, J. Phys. IV France **7**, C2-753 (1997).

[40] P. J. Brown, A. G. Fox, E. N. Maslen, M. A. O'Keefe, and B. T. M. Willis, Intensity of diffracted intensities, *International Tables for Crystallography*, Vol. C (2006), Chap. 6.1, p. 554.

[41] C. T. Chantler, K. Olsen, R. A. Dragoset, J. Chang, A. R. Kishore, S. A. Kotochigova, and D. S. Zucker, Detailed tabulation of atomic form factors, photoelectric absorption and scattering cross section, and mass attenuation coefficients for Z = 1-92 from E = 1-10 eV to E = 0.4-1.0 MeV, https://www.nist.gov/pml/x-ray-form-factor-attenuation-and-scattering-tables.

[42] V. Cherepanov, I. Kolokolov, and V. L'vov, The saga of YIG: Spectra, thermodynamics, interaction and relaxation of magnons in a complex magnet, Phys. Rep. **229**, 81 (1993).

[43] M. Bonnet, A. Delapalme, H. Fuess, and M. Thomas, Refinement of the structure of yttrium iron garnet (YIG). A case of severe extinction and absorption, Acta Cryst. B Struct. Cryst. Cryst. Chem. **B31**, 2233 (1975).

[44] J. Strempfer, S. Francoual, D. Reuther, D. K. Shukla, A. Skaugen, H. Schulte-Schrepping, T. Kracht, and H. Franz, Resonant scattering and diffraction beamline P09 at PETRA III, J. Synchrotron Rad. **20**, 541 (2013).

[45] S. D. Brown, L. Bouchenoire, D. Bowyer, J. Kervin, D. Laundy, M. J. Longfield, D. Mannix, D. F. Paul, A. Stunault, P. Thompson, M. J. Cooper, C. A. Lucasa, and W. G. Stirlinga, The XMAS beamline at ESRF: Instrumental developments and high-resolution diffraction studies, J. Synchrotron Rad. **8**, 1172 (2001).

[46] M. Kamiński, Studying magnetism with x-ray standing waves, Ph.D. thesis, University of Hamburg, 2022.

[47] S. Francoual, J. Strempfer, D. Reuther, D. K. Shukla, and A. Skaugen, Double phase-retarder set-up at beamline P09 at PETRA III, J. Phys.: Conf. Ser. **425**, 132010 (2013).

[48] J. Strempfer, J. R. L. Mardegan, S. Francoual, L. S. I. Veiga, L. Bouchenoire, T. Spitzbart, and H. Zink, Fast helicity switching of x-ray circular polarization at beamline P09 at PETRA III, AIP Conf. Proc. **1741**, 030017 (2016).

[49] J. Goulon, A. Rogalev, F. Wilhelm, N. Jaouen, C. Goulon-Ginet, G. Goujon, J. B. Youssef, and M. V. Indenbom, X-ray detected magnetic resonance at the Fe K-edge in YIG: Forced precession of magnetically polarized orbital components, JETP. Lett. **82**, 696 (2005).

[50] A. Rogalev, J. Goulon, F. Wilhelm, C. Brouder, A. Yaresko, J. B. Youssef, and M. V. Indenbom, Element selective x-ray magnetic circular and linear dichroisms in ferrimagnetic yttrium iron garnet films, J. Magn. Magn. Mater. **321**, 3945 (2009).

[51] S. Hosseinzadeh, M. Behboudnia, L. Jamilpanah, M. H. Sheikhi, E. Mohajerani, K. Tiane, A. Tiwari, P. Elahi, and S. M. Mohseni, High saturation magnetization, low coercivity and fine YIG nanoparticles prepared by modifying co-precipitation method, J. Magn. Magn. Mater. **476**, 355 (2019).